INORGANIC CHEMISTRY FRONTIERS

RESEARCH ARTICLE

View Article Online
View Journal | View Issue

Cite this: *Inorg. Chem. Front.*, 2023, **10**, 5734

Enhanced performance of perovskite solar cells *via* a bilateral electron-donating passivator as a molecule bridge†

Weichun Pan,‡[a] Pengxu Chen,‡[a] Sijia Zhu,[a] Ruowei He,[a] Qingshui Zheng,[a] Fengxian Cao,[a] Zhang Lan,[a] Jihuai Wu,*[a] Weihai Sun*[a] and Yunlong Li*[b]

Defects at the buried interface are the primary factors contributing to recombination losses and instability in perovskite solar cells (PSCs) with n–i–p structure. Here, a molecule with bilateral electron-donating groups, 6-amino-1-hexanol (HAL), is introduced between SnO_2 and perovskite (PVK) to optimize the characteristics of the buried interfacial properties, as well as the PVK film quality. The surface defects of SnO_2 can be more effectively passivated, and its energy level structure can be tuned more appropriately. Meanwhile, the electron-donating groups in HAL can passivate the Pb^{2+} defects and stabilize the $[PbI_6]^{4-}$ octahedra at the buried interface. With the assistance of bilateral electron-donating groups, HAL can act as a molecular bridge to easily bridge SnO_2 and PVK to passivate the buried interfacial defects, thus enhancing device performance. As a result, the photovoltaic performance was significantly improved by the buried modification with HAL, ultimately achieving a champion PCE of 23.58%, far superior to the inferior PCE of 21.30% of the pristine device. Furthermore, after 35 days of storage at approximately 35% relative humidity (RH) and room temperature, the device based on HAL-modified SnO_2 demonstrates significantly better stability than the pristine device, as it still maintains over 90% of the initial efficiency. This study provides an effective molecular bridge strategy for further enhancing the performance of PSCs.

Received 3rd August 2023,
Accepted 23rd August 2023

DOI: 10.1039/d3qi01531a

rsc.li/frontiers-inorganic

1. Introduction

Since the excellent photovoltaic performance of perovskites (PVK) has been widely acknowledged, extensive research has been conducted on perovskite solar cells (PSCs) with the hope that they may serve as the next-generation replacement for silicon-based solar cells. In recent years, the power conversion efficiency (PCE) of PVK-based photovoltaic devices has significantly increased, from only 3.8% to over 25% certified PCE.[1–12]

For PSC devices with n–i–p structure, the quality of the electron transport layer (ETL) is a crucial factor in achieving stable and efficient normal PVK devices. This is because the incoming light must pass through the ETL before reaching the PVK layer, making it crucial to select the ETL to match the PVK layer rationally.[13] Inorganic ETLs, with the advantages of low cost, high stability, and facile process technology, have been regarded as the most promising electron transport materials for preparing high-performance PSCs.[14] The most widely employed inorganic electron transport materials in normal PSCs include SnO_2, TiO_2, ZnO, and so on.[14] The PSCs based on TiO_2 and SnO_2 ETLs have both demonstrated high PCE exceeding 25%.[12,15] Notably, SnO_2 may be more promising than TiO_2 due to its non-photocatalytic activity and low-temperature processability.[14,16] Inevitably, SnO_2 also has certain disadvantages, such as oxygen vacancies and Sn interstitial defects on its surface, which serve as non-radiative recombination centers resulting in recombination losses.[17,18] Moreover, the construction of efficient and stable SnO_2-based PSCs also requires high-quality PVK thin films. Simultaneously, solution-processed PVK films will generate high defect densities, which adversely affects film quality and surface contact and is a limiting factor in achieving further device performance improvements.[19,20] Generally, the deep-level defect concentration at the buried interface of PVK is much higher than that at the upper surface, which not only hampers electron transport but also severely impedes the crystal growth of the PVK layer.[21,22] Therefore, the buried interfacial defects will impede the enhancement of open-circuit voltage (V_{OC}) and fill factor

[a]*Engineering Research Center of Environment-Friendly Functional Materials, Ministry of Education, Institute of Materials Physical Chemistry, College of Materials Science & Engineering, Huaqiao University, Xiamen, 361021, China. E-mail: jhwu@hqu.edu.cn, sunweihai@hqu.edu.cn*

[b]*Shenzhen Institute of Advanced Technology Chinese Academy of Sciences, Shenzhen, China. E-mail: yl.li2@siat.ac.cn*

†Electronic supplementary information (ESI) available. See DOI: https://doi.org/10.1039/d3qi01531a

‡These authors contributed equally to this work.

(FF) in PSCs.[23] Presently, the introduction of a functional molecule that can exert positive influences on both SnO_2 and PVK simultaneously remains a significant challenge. To tackle this challenge, many researchers have been inclined to investigate the optimization of the buried interface of PVK.[17,24–27] Clearly, the buried interfacial modification has emerged as an effective strategy for achieving high-efficiency PSCs with n–i–p structure.

Herein, we introduced a bilateral electron-donating groups passivator (6-amino-1-hexanol, HAL) as a molecular bridge at the buried interface of PSCs aiming to simultaneously regulate the surface defects of SnO_2 and the quality of PVK films. The HAL with the bilateral electron-donating groups can effectively mitigate surface defects on SnO_2 to suppress carrier recombination. Meanwhile, the presence of HAL on the SnO_2 surface is beneficial for improving energy-level structure and increasing electron donor species, which ultimately enhances electron extraction and transport. Furthermore, the improved surface wettability of SnO_2 films facilitates the formation of large PVK grains with low defect densities. Benefiting from the presence of electron-donating groups, the surface properties of SnO_2 are positively regulated, and the quality of PVK films is effectively improved. As a result, compared to the pristine device (21.30%,) the n–i–p structured PSCs based on HAL-modified SnO_2 achieved a significant improvement, with a champion PCE of up to 23.58%. More importantly, the unencapsulated devices modified with HAL maintained over 90% of the initial PCE after aging for 35 days at approximately 35% relative humidity (RH). The present work demonstrates that molecules with bilateral electron-donating groups can act as molecular bridges at the buried interface of the SnO_2-based PSCs, positively enhancing device performance.

2. Results and discussion

The buried interfacial modification was used to introduce a linear organic molecule (6-amino-1-hexanol, HAL) between SnO_2 and PVK, whose chemical structure (Fig. S1†) has two functional groups, amino ($-NH_2$) and hydrocarbon (–OH) groups. To confirm the possibility of HAL interacting with SnO_2 and PVK, we simulated the electrostatic potential (ESP) of HAL. From Fig. S2,† it can be observed that the high charge distribution of $-NH_2$ and –OH groups in the HAL molecule indicates that the $-NH_2$ and –OH groups of HAL are expected to passivate the oxygen vacancies of SnO_2. More importantly, according to previous works, the uncoordinated $Pb^{2+}$of the $[PbI_6]^{4-}$ octahedral and the electron-donating groups ($-NH_2$/–OH) could form Lewis adducts through the interaction between the lone-pair electrons in them, and the formation of Lewis acid–base pairs of Pb^{2+} with electron-donating groups helps to stabilize the $[PbI_6]^{4-}$ octahedra.[28–30] Furthermore, the $-NH_2$ and –OH groups of HAL can connect with the iodide from $[PbI_6]^{4-}$ octahedra *via* H-bond formation, which is also beneficial for the stabilization of $[PbI_6]^{4-}$ octahedra at the buried interface of PVK.[31–33]

To investigate the effect of introducing HAL as a modifier on SnO_2, the analytical results for the characterization using X-ray photoelectron spectroscopy (XPS) can be depicted in Fig. 1a–c and Fig. S3.† From the N 1s spectra (Fig. 1a) of pristine SnO_2 and HAL-modified SnO_2, the appearance of N 1s peaks in HAL-modified SnO_2 can confirm the presence of HAL on the SnO_2 surface, which is not present in the pristine films. The positions of the double peaks representing Sn $3d_{2/3}$ and Sn $3d_{2/5}$ in the Sn 3d patterns (Fig. 1b) of the HAL-modified SnO_2 films are shifted by 0.27 eV toward the low binding energy position relative to the pristine SnO_2, which implies an enhancement of the electron cloud density. The change in electron cloud density may be attributed to the fact that the nitrogen in $-NH_2$ and oxygen in –OH with lone pairs of electrons can coordinate with the uncoordinated Sn^{4+} in SnO_2, which induces electron transfer from nitrogen and oxygen elements in HAL to SnO_2.[34,35] The result of Sn 3d spectra confirms the existence of interaction between HAL and SnO_2. From the O 1s spectra in Fig. 1c, an asymmetric peak profile appears in both pristine SnO_2 and HAL-modified SnO_2 films. The O 1s peaks of all samples can be deconvoluted into two peaks, the peak at 530.67 eV belongs to lattice oxygen ($O_{Lattice}$), and the peak at 531.93 eV originates from vacancy oxygen ($O_{Vacancy}$). Utilizing the $O_{Vacancy}/(O_{Lattice} + O_{Vacancy})$ formula in conjunction with analysis of the O 1s spectra, we can calculate the peak area ratio for $O_{Vacancy}$.[34] The calculated results showed that the peak area ratio of $O_{Vacancy}$ decreased from 0.43 to 0.38 for the HAL-modified SnO_2 sample compared with the pristine SnO_2 sample. This result proves that HAL can effectively passivate the oxygen vacancies, thus inhibiting defect-induced non-radiative recombination at the SnO_2/PVK interface.

The interaction between HAL and SnO_2 motivated us to further investigate the influence of SnO_2 modification on the properties of SnO_2 films. From Fig. S4,† the UV-Vis transmission spectra demonstrate that the modification of HAL did not affect the high transmittance of the SnO_2 films. The UV-vis absorption spectroscopy (Fig. S5†) measurements of different SnO_2 films were also performed and converted into the Tauc plots. From the Tauc plots in Fig. S6,† the band gap (E_g) of the SnO_2 film was not altered by the introduction of HAL, and the E_g of the HAL-modified SnO_2 film remained at 3.91 eV. Furthermore, possibly attributed to the presence of the electron-donating groups ($-NH_2$/–OH) with lone pairs of electrons, the Tafel curves of different devices in Fig. S7† reveal that the HAL-modified sample exhibits higher electrical conductivity than the pristine sample.

At the same time, the ultraviolet photoelectron spectroscopy (UPS) technique was also used to investigate whether the interaction of HAL with SnO_2 changed the energy-level structure of SnO_2/HAL. Fig. 1d and e exhibit the UPS spectra of pristine and HAL-modified SnO_2 films, respectively. Based on the data of the onset (E_{oneset}) and the secondary electron cutoff (E_{cutoff}) of the UPS spectra, the conduction band minimum (E_{CBM}), work function (W_F), and valence band maximum (E_{VBM}) of the samples can be arithmetically derived.[36] The detailed para-

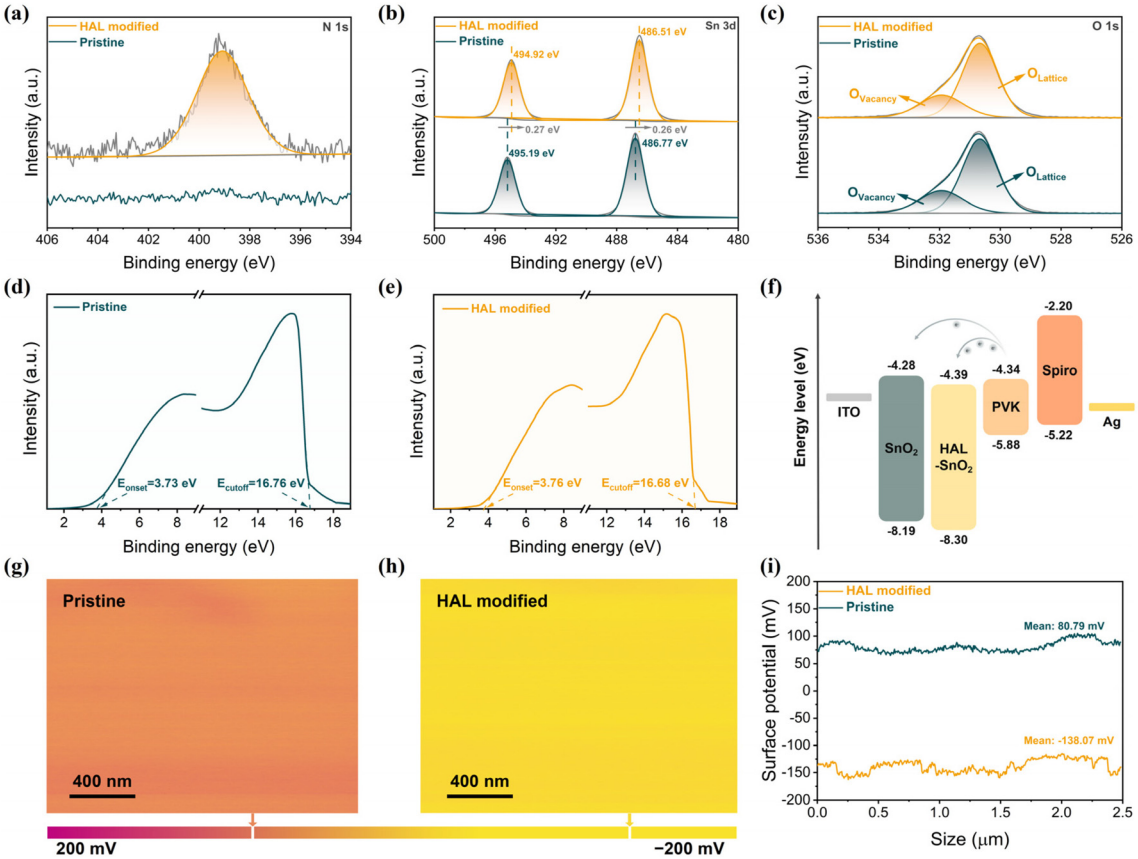

Fig. 1 (a) N 1s, (b) Sn 3d, and (c) O 1s XPS spectra of different SnO_2 films. UPS spectra of (d) SnO_2 and (e) HAL-modified SnO_2 films. (f) Energy band diagram of the materials employed in PSCs. KPFM images of (g) SnO_2 and (h) HAL-modified SnO_2 films. (i) Surface potential of different SnO_2 films.

meters of the energy level for the samples are displayed in Table S1.† Combining the data obtained from UPS analysis and the energy level distribution from previous literature, we plotted the corresponding energy band diagrams in Fig. 1f.[36] It is noteworthy from Fig. 1f that the E_{CBM} of the pristine and HAL-modified SnO_2 films are −4.28 eV and −4.39 eV, respectively. Compared to the E_{CBM} (−4.34 eV) of PVK, the pristine SnO_2 film with a higher E_{CBM} (−4.28 eV) would hinder electron transport and induce carrier accumulation at the buried interface. In contrast, the HAL-modified SnO_2 film with a lower E_{CBM} (−4.39 eV) than that of PVK would be more favourable for electron transport and extraction between SnO_2 and PVK. The analytical results based on UPS measurements illustrate that the modification of HAL can construct a smoother energy gradient between SnO_2 and PVK, which facilitates the reduction of energy loss and the enhancement of photovoltage. More importantly, the HAL-modified SnO_2 film with a deeper E_{VBM} can create a higher energy barrier for hole injection at the SnO_2/PVK interface, further suppressing the loss of charge recombination. Additionally, surface electronic properties of SnO_2 films were assessed for various samples by measuring their contact potential difference (CPD) using Kelvin probe force microscopy (KPFM) techniques. From Fig. 1g–i, it can be noted that the HAL-modified SnO_2 film has a lower average CPD of −138.07 mV than the pristine SnO_2 film (80.79 mV). The reduction in CPD may be attributed to the increased number of electron donor species associated with the introduction of HAL, which would result in an increase in the film work function, in agreement with the findings from UPS analysis.

For devices with n–i–p structures, the surface properties of SnO_2 films profoundly affect the quality of the deposited PVK films. To determine the influence of HAL modification on the morphology of SnO_2 films, we measured the films using scanning electron microscopy (SEM) and atomic force microscopy (AFM). From Fig. S8,† it can be observed that there is significant agglomeration on the pristine SnO_2 film. In contrast, there is no significant agglomeration on the HAL-modified SnO_2 film. As seen from the AFM images of Fig. S9,† the surface of HAL-modified SnO_2 is flatter and more uniform, and the roughness of the modified SnO_2 is significantly reduced relative to the pristine SnO_2, which contributes to the interfacial contact between SnO_2 and PVK.[20] Besides, the contact angle tests were performed on the pristine and HAL-modified SnO_2 films using the DMF/DMSO mixture solution, as illustrated in Fig. S10.† Compared to ITO/SnO_2 (20°), the DMF/DMSO mixture solution had a smaller contact angle (8°) on ITO/SnO_2/HAL. The smaller the contact angle between the

DMF/DMSO mixture solution and the substrate, the smaller the Gibbs free energy required for nucleation.[37] The above analyses demonstrate that the modification of HAL is more favorable to the nucleation of PVK and the improvement of the interfacial contact between PVK and SnO_2.

To further verify that the introduction of HAL can ameliorate the quality of PVK films, we also measured the top-view and cross-sectional SEM images of samples with ITO/SnO_2 (without and with HAL)/PVK structures. From Fig. 2a and b, it can be seen that the PVK film of the HAL-modified sample has a flatter surface, more blurred grain boundaries, and larger grain size relative to the pristine sample. The cross-sectional SEM images (Fig. 2d and e) also directly verify the results of the top-view SEM images with better quality for the PVK films with HAL-modified SnO_2. The surface roughness of PVK films based on different ETL substrates was analyzed using AFM measurements. It is known from Fig. S11† that the roughness (28.5 nm) of PVK film on the HAL-modified SnO_2 is lower compared to the pristine PVK film (38.3 nm). The smaller the roughness of the PVK surface, the more favorable the contact at the PVK/HTL interface.[20] This phenomenon contributes to the extraction and transfer of holes from PVK to HTL.

From the XRD patterns in Fig. 2c, it can be noted that the modification of HAL did not alter the crystal structure of PVK. However, the (110) crystalline plane of the PVK films with HAL-modified SnO_2 has a stronger diffraction peak intensity, which indicates that the modification of HAL improved the crystalline intensity of PVK. The XRD results are consistent with the SEM analysis. Additionally, UV-Vis absorption spectroscopy measurements were also used to determine the absorption of PVK films based on different substrates. Due to the improved quality of the PVK films, it can be noted from Fig. 2f that the PVK film with HAL-modified SnO_2 displays a higher absorption intensity in the range of 400–600 nm, which indicates that the buried modification of HAL has a positive effect on the PVK films. As shown in the Tauc plots of Fig. S12† obtained from the conversion of Fig. 2f, we find that the E_g of the PVK film does not change due to the modification of HAL. Further, we obtained the corresponding plots (Fig. S13†) of Urbach energy (E_U) from the UV-Vis absorption spectra. The E_U is a specific physical parameter that is related to the crystallinity, trap states, and electronic disorder of the material, from which we can infer the PVK film quality. From Fig. S13,† the obtained data reflect that the PVK film with the HAL-modified SnO_2 has a lower E_U (37.74 meV) relative to the pristine samples (46.95 meV). The smaller the E_U, the better the PVK film quality.[38] The result of E_U is consistent with our previous findings, which prove that the modification of HAL can effectually enhance the quality of PVK films and suppress the defect states.

The improved quality of PVK films leads us to consider whether there is also an interaction between HAL and PVK. The XPS spectra based on the PbI_2 films without and with HAL are shown in Fig. 3a and b. It can be observed from the Pb 4f spectra in Fig. 3a that after the introduction of HAL, the double peaks on behalf of Pb $4f_{7/2}$ and Pb $4f_{5/2}$ are overall shifted towards the lower binding energy by 0.21 eV compared to the pristine films. The variation of the binding energy in the Pb 4f caused by the HAL modification demonstrates the presence of an interaction between HAL and PbI_2. Furthermore, the two shoulder peaks representing Pb^0 are more obvious on the pristine PVK film than on the PVK film based on the HAL-modified SnO_2, implying that the presence of HAL can inhibit the Pb^0 defects. From the I 3d spectra in Fig. 3b, the I $3d_{5/2}$ and $3d_{3/2}$ peaks are shifted by 0.36 eV overall toward the lower binding energy relative to the pristine

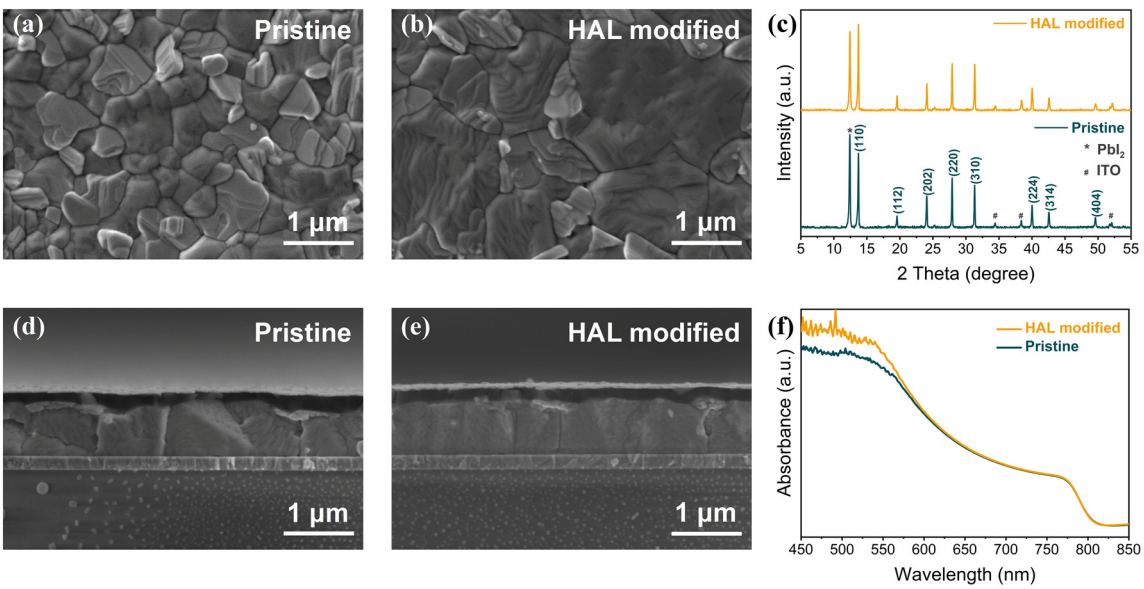

Fig. 2 Top-view SEM images of PVK films with (a) pristine and (b) HAL-modified SnO_2 films. (c) XRD patterns and (f) UV-Vis absorption spectra of PVK films with different SnO_2 films. Cross-sectional SEM images of PSC devices with (d) pristine and (e) HAL-modified SnO_2 films.

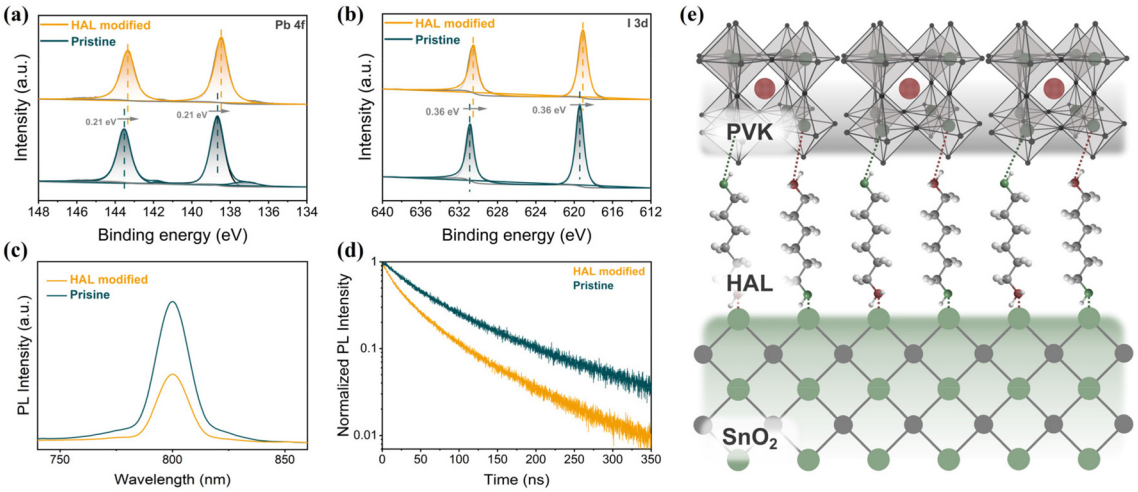

Fig. 3 (a) Pb 4f and (b) I 3d XPS spectra of PbI_2 films based on different SnO_2 films. (c) SSPL and (d) TRPL spectra of PVK films based on different SnO_2. (e) Schematic diagram illustrating potential interaction mechanisms for the buried interfacial modification of HAL.

film. The observed shift in the I 3d XPS spectra suggests that the interaction between HAL and PbI_2 may have resulted in a decrease in the oxidation state of iodide or weakening of the Pb–I bond.[39] The interaction of HAL and PbI_2 may be attributed to the existence of the electron-donating groups (–NH_2/–OH) with lone pairs of electrons in HAL. As illustrated in Fig. 3f, we have drawn the relevant schematic diagrams to demonstrate the buried modification of HAL more intuitively. Due to the electron-donating groups with lone pairs of electrons on HAL, the introduction of HAL can effectually passivate the surface defects on SnO_2 and improve the contact at the SnO_2/PVK interface. Meanwhile, the electron-donating groups of HAL can modulate the uncoordinated Pb^{2+} defects and stabilize $[PbI_6]^{4-}$ octahedra at the bottom interface of PVK through this coordination and hydrogen bonding.

To clarify the effect of the buried modifications of HAL on the carrier dynamics of the SnO_2/PVK interface, the steady-state photoluminescence (SSPL) and time-resolved photoluminescence (TRPL) measurements of the samples with ITO/SnO_2 (without and with HAL)/PVK structures were revealed in Fig. 3c and d, respectively. In the SSPL spectra in Fig. 3c, it can be found that the sample with the introduction of HAL for the modification obviously exhibits a lower steady-state PL intensity than the samples without the introduction of HAL, which suggests a more efficient extraction and transport of photogenerated electrons at the SnO_2/PVK interface. The carrier extraction lifetimes of different samples were determined by fitting the TRPL plots shown in Fig. 3d with a bi-exponential decay equation, and the detailed fitted data are displayed in Table S2.†[34] Compared with the pristine sample, the average carrier lifetime of the HAL-modified sample is lower, proving that the HAL modification favors the transport of photo-generated electrons from PVK to SnO_2. The reduction in the average carrier lifetime of the sample with the ITO/SnO_2/HAL/PVK structure corresponds to the reduced steady-state PL intensity. These findings strongly confirm that the introduction of HAL can effectually reduce the defects of SnO_2 and PVK and improve electron extraction and transport by suppressing the non-radiative recombination, ultimately improving V_{OC} and FF in the device.

Measuring the impact of buried modifications on improving performance using a complete device with n–i–p structure is necessary. Fig. 4a shows that the leakage current of the PSC with HAL is smaller than the pristine PSC. The decrease in dark current suggests that the introduction of HAL can effectively mitigate current leakage, improving the J_{SC} and FF of the PSCs.[40] Electrochemical impedance spectroscopy (EIS) was employed to acquire additional information on carrier transport behavior and interfacial properties. The Nyquist plots of the PSC devices at 1.0 V bias voltage were acquired under AM 1.5 G solar irradiation conditions. The corresponding equivalent circuit diagram is marked in Fig. 4b, and the fitted measurement parameters are listed in Table S3.† The Nyquist plot is made up of two semicircles that are located in different frequency ranges. In impedance measurements, the high-frequency component usually indicates the charge transfer resistance (R_{ct}), while the low-frequency component is typically associated with the complex resistance (R_{rec}).[39] Relative to the pristine device, the HAL-modified device exhibits a significant decrease in R_{ct} coupled with a marked increase in R_{rec}, which demonstrated that the introduction of HAL can effectively enhance carrier extraction and transfer, as well as inhibit carrier recombination at the ETL/PVK interface.

From the light-intensity-dependent V_{OC} measurement in Fig. 4c, the device with HAL displays a smaller slope (1.22 kT q^{-1}) compared to the pristine device (1.52 kT q^{-1}). The deviation of the slope from unity (kT q^{-1}) is a well-established metric that reflects the presence of trap-assisted non-radiative recombination in PSCs. The lower value for the HAL-modified device indicates a reduction in non-radiative recombination.[18] This result implies that the HAL modification strategy may lead to improved performance and stability of PSCs by redu-

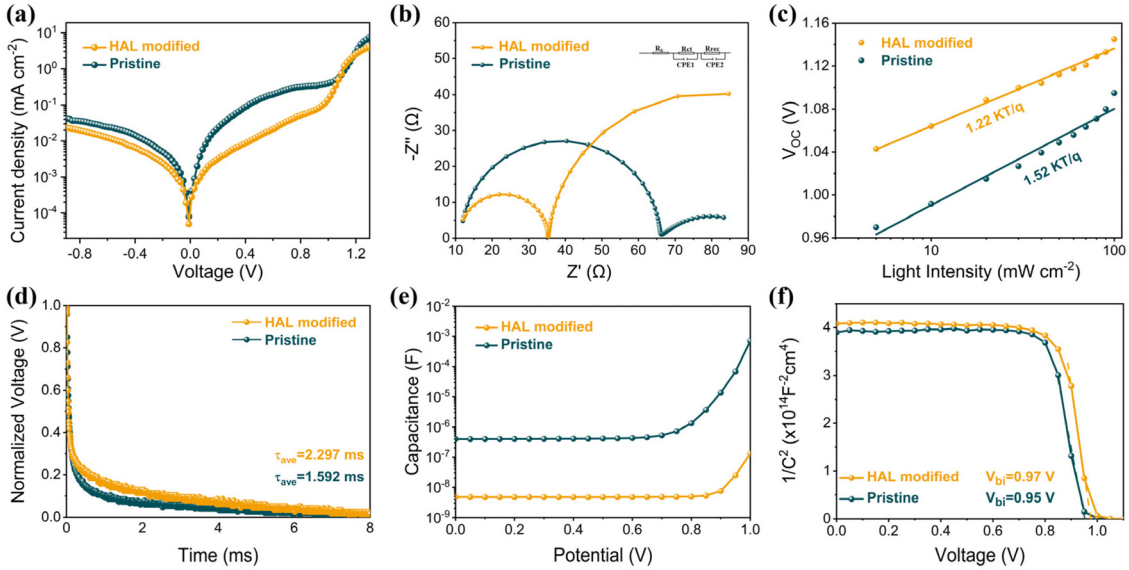

Fig. 4 (a) The dark-state *J*–*V* curves, (b) Nyquist plots, (c) Light-intensity-dependent V_{OC} curves, (d) TPV curves, (e) *C*–*V* curves, and (f) *M*–*S* curves for PSCs based different SnO_2 films.

cing the energy losses attributed to non-radiative recombination. In addition, the transient photovoltage (TPV) measurements of the device further confirm that the introduction of HAL promotes the carrier transfer and suppresses the recombination, and the results are shown in Fig. 4d. After introducing HAL, the decay rate of TPV slows down, indicating a longer carrier lifetime, which is associated with reduced non-radiative interfacial recombination.[21] In other words, the introduction of HAL can effectively passivate defect-induced recombination to achieve faster carrier transport and longer carrier lifetime.

Fig. 4e shows the Capacitance–Voltage (*C*–*V*) plots of the devices with different ETLs. It can be clearly seen that the capacitance of the device with HAL is much smaller than that of the pristine, which proves that the presence of HAL can reduce the charge accumulation at the buried interface.[36] The Mott–Schottky (*M*–*S*) curves presented in Fig. 4f clearly demonstrate that the built-in potential (V_{bi}) of the device with HAL is significantly greater than that of the original device. The increase of V_{bi} means a stronger electric field between ETL and PVK, which is beneficial for enhanced carrier separation and extraction.[40] These properties promote the charge collection, increasing the FF and contributing to higher V_{OC}.

Fig. 5a illustrates the device structure of PSCs with n–i–p structure in this work, where HAL is inserted between SnO_2 and PVK layers by the buried modification. The positive effects of HAL on the passivation of SnO_2 defects, the tuning of energy levels, and the promotion of PVK crystallization are bound to have an impact on the photovoltaic performance of PSCs. To further explore the optimal concentration of HAL for efficient PSCs, we set up concentration gradients of 0, 0.5, 1.0 and 1.5 mg mL^{-1} and assembled the complete devices. The *J*–*V* curves revealing the impact of different HAL concentrations on the performance of devices are displayed in Fig. S14,† and the detailed corresponding parameters are listed in Table S4.† From the data collected from the *J*–*V* curves, we can find that the optimal HAL concentration is 1.0 mg mL^{-1}. Fig. 5b illustrates a comparison of the PCE between the champion and pristine devices, revealing the superior performance of the champion device. The champion device can achieve a PCE of 23.58% (with a V_{OC} of 1.155 V, FF of 0.8227, and J_{SC} of 24.82 mA cm^{-2}), which is significantly higher than the pristine device with a PCE of 21.30%, V_{OC} of 1.110 V, FF of 0.7861, and J_{SC} of 24.41 mA cm^{-2}. The EQE spectrum (Fig. S15†) of the device with HAL demonstrates an integrated current density of 24.40 mA cm^{-2}, which matches the measurement results obtained from the *J*–*V* characterization. To determine the reproducibility of the devices, we selected 20 devices from each of the HAL-modified devices and pristine devices, and further evaluated the statistical distribution of the collected photoelectric data, which corresponding statistical data are listed in Table S5.† As shown in Fig. 5c and Fig. S16,† HAL-modified devices exhibit superior photoelectric performance over the pristine devices, especially higher PCE and more concentrated PCE distribution, which is primarily benefiting from the improvement in V_{OC} and FF.

The improvement of photoelectric performance affirms the positive effect of the HAL buried modification, and this enhancement may be due to the effective defect passivation of HAL. To further investigate the impact of HAL on the defects of devices, we employed the trap density of states (tDOS) of different devices. As shown in Fig. 5d, the tDOS spectra contain three distinct types of trap states, corresponding to the three energy bands (labeled as band 1, band 2, and band 3).[41] It is evident that the overall tDOS of the HAL-modified device is lower than that of the pristine device, especially the tDOS of the HAL-modified device at shallow energy levels (band 1) is considerably lower than that of the pristine device. The traps belonging to band 1 at the low-energy region are usually

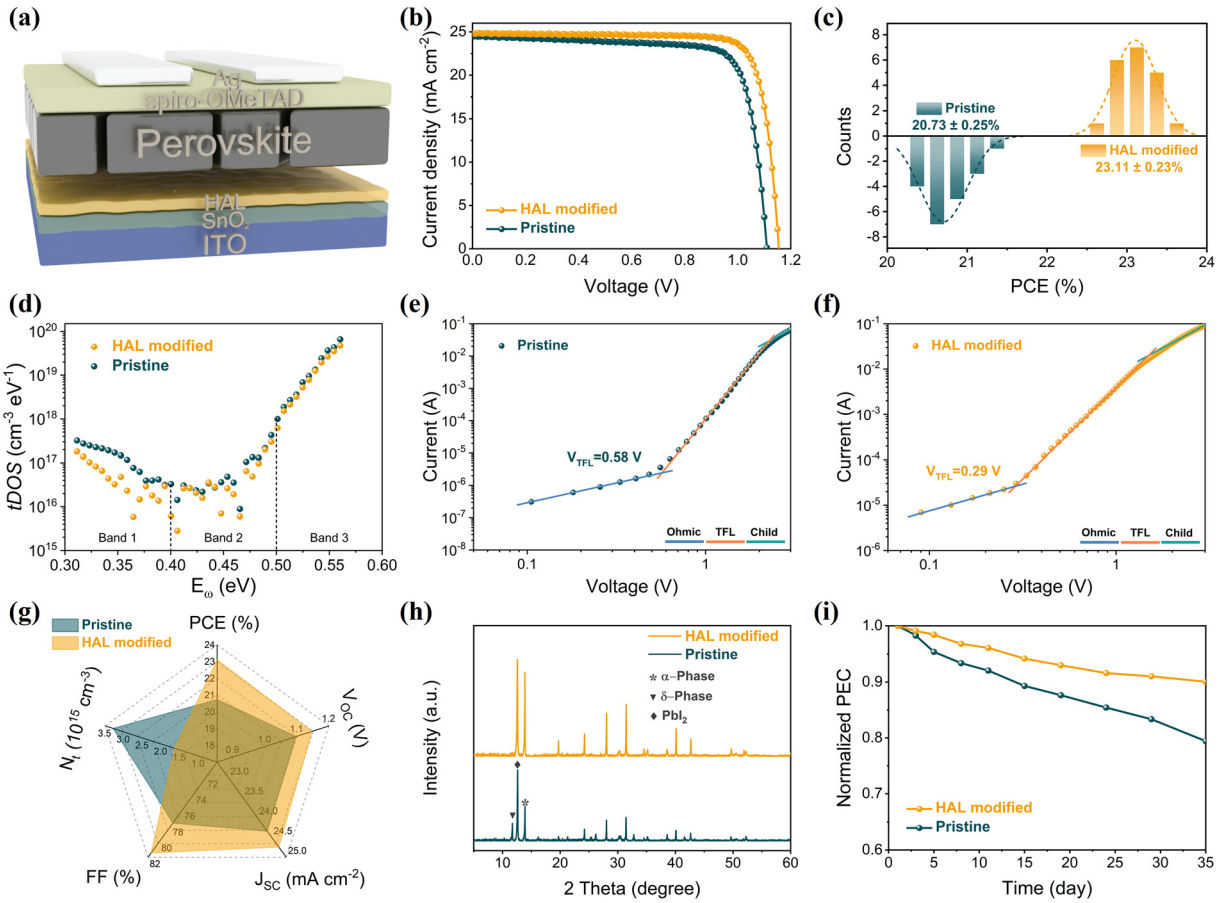

Fig. 5 (a) Schematic device structure of PSCs with HAL-modified SnO_2. (b) The *J*–*V* curves, (c) PCE histograms, and (d) tDOS spectra of PSCs with different SnO_2 films. The SCLC curves for electron-only devices with (e) pristine and (f) HAL-modified SnO_2. (g) Radar graph of average photoelectric parameters of PSCs with different SnO_2 films. (h) XRD stability and (i) PCE stability of PSCs with different SnO_2 films in an air environment with a RH of about 35%.

associated with iodide vacancies at grain boundaries, indicating that the introduction of HAL can effectively reduce the trap states associated with vacancies at grain boundaries.[9,41] The reduction of the defects at the shallow energy level may be attributed to the fact that the bilateral electron-donating groups of HAL can coordinate with uncoordinated Pb^{2+} to stabilize the $[PbI_6]^{4-}$ octahedra at the buried interface.

Moreover, we further evaluated the defect states of PSCs before and after modification using the space-charge-limited current (SCLC) technique for electron-only devices with ITO/SnO_2/PVK/PCBM/Ag structures. It is well known that the trap-filled limit voltage (V_{TFL}) is positively related to the trap density (N_{trap}). The smaller the V_{TFL}, the smaller the N_{trap}.[12,40] From the dark-state *J*–*V* curves of Fig. 5e and f, the V_{TFL} values for the HAL-modified and pristine electron-only devices are 0.29 V and 0.58 V, respectively. By calculation, it is known that the N_{trap} of the HAL-modified device (1.64×10^{15} cm^{-3}) is smaller than that of the pristine device (3.29×10^{15} cm^{-3}), which also proves that HAL is effective for defect passivation. The Radar graph (Fig. 5g) is used to provide a more visual analysis of the average photovoltaic parameters of the HAL-modified and pristine devices, and it is clear that the HAL-modified device has a lower N_{trap} than the pristine devices, resulting in better photovoltaic performance.

The positive role of HAL in photovoltaic performance prompted us further to investigate its influence on the stability of PSCs. As shown in Fig. 5h, the XRD technique was utilized to monitor the degradation state of the PVK films. After 35 days of storage in air at 35% RH, the (110) peak of PVK in the pristine film has significantly degraded, while the PbI_2 and δ-phase peaks have increased noticeably. In contrast, the phase transition of the PVK film with HAL-modified SnO_2 has hardly increased with time. The degradation in the pristine devices can be ascribed to the large amounts of defects in the PVK films, which induce the degradation of the PVK films. In addition, we assess the long-term stability of HAL-modified and pristine devices in an air storage environment (RH of ~35%, temperature of ~25 °C). From Fig. 5i, the HAL-modified device has a lower decay rate than the pristine device during the 35-day stability test. After 35 days, the HAL-modified device still retained more than 90% of the initial PCE, whereas the pristine device only retained 79% of the initial PCE. The improved stability may be benefit from the fact that the buried modification of HAL not only effectually passivates the defects

at the SnO_2/PVK interface but also stabilizes $[PbI_6]^{4-}$ octahedra by the interactions to stabilize the perovskite structure.

3. Conclusion

In summary, an effective molecular bridge strategy is developed to positively modulate the buried interface in SnO_2-based PSCs. Owing to the bilateral electron-donating groups (–NH_2/–OH), HAL can act as a molecular bridge to passivate the defects on the SnO_2 surface and simultaneously improves the quality of PVK films. Modification of SnO_2 with HAL results in lower defect density and improved energy level matching, which is beneficial for electron extraction and transport. Furthermore, the presence of electron-donating groups on HAL-modified SnO_2 promotes the formation of low-defect PVK films and stabilizes the buried interface of PVK through interactions, which facilitates the suppression of interfacial defects and the reduction of voltage loss. Consequently, PSCs with HAL-modified SnO_2 achieve a high PCE of 23.58%, which is significantly higher than that of the pristine PSCs. Benefiting from the reduction of defects, PSCs based on HAL-modified SnO_2 have exhibited superior stability compared to the pristine PSCs. After storing under approximately 35% RH for 35 days, the HAL-modified SnO_2-based PSCs maintain more than 90% of the initial efficiency. This work demonstrates an effective molecular bridge strategy to optimize the buried interface in n–i–p PSCs, which further improves the performance and stability of PSCs.

4. Experimental sections

4.1 Materials

SnO_2 hydrocolloid solution (15 wt%) was purchased from Alfa Aesar. Indium tin oxide (ITO, 14 Ω sq^{-1}), methylamine hydrochloride (MACl, 99.5%), methylammonium iodide (MAI, 99.5%), and formamidinium iodide (FAI, 99.9%) were purchased from Advanced Election Technology Co., Ltd. Lead iodide (PbI_2, 99.99%) was purchased from Xi'an Polymer Light Technology Corp. 2,2′,7,7′-Tetrakis(*N*,*N*-di-*p*-methoxyphenylaMino)-9,9′-spirobifluorene (Spiro-OMeTAD, 99.8%) was purchased from Shenzhen Feiming Science and Technology Co., Ltd. Chlorobenzene(CB, 99%), acetonitrile (ACN, 99%), dimethyl sulfoxide (DMSO, 99.7%), isopropanol (IPA, 99.5%), 4-*tert*-butylpyridine (*t*-BP, 98%), dimethylformamide (DMF, 99.8%), and bis(trifluoromethane) sulfonimide lithium salt (Li-TFSI, 99.95%) were purchased from Sigma-Aldrich. All chemicals and solvents are used directly without further purification.

4.2 Device fabrication

To attain a substrate with optimal cleanliness, the ITO glass substrate ought to undergo sequential sonication using IPA, acetone, and ethanol, each for 15 min. After the washing process, the glass should be dried under a stream of nitrogen gas and subsequently subjected to a combined UV-ozone and plasma treatment for 30 minutes. The SnO_2 hydrocolloid solution needs to be further diluted with deionized water at a volume ratio of 1 : 4 and then sonicated for 15 min to ensure homogeneous mixing. The diluted SnO_2 hydrocolloid solution was spin-coated onto the ITO substrate at 3500 rpm for 25 s and subsequently heat-treated at 150 °C for 30 min to gain ETL. Different concentrations of HAL aqueous solutions (0.5 mg mL^{-1}, 1.0 mg mL^{-1}, and 1.5 mg mL^{-1}) were equipped as needed. The HAL modification solution was spin-coated onto the prepared SnO_2 ETLs at 4000 rpm for 25 s, followed by heat treatment at 130 °C for 25 min to gain HAL-modified SnO_2 ETLs. The $FA_{0.92}MA_{0.08}PbI_3$ light-absorbing layer was formed by a simple two-step method. Under a nitrogen atmosphere, a PbI_2 solution (1 : 9 volume ratio of DMSO to DMF) with a concentration of 1.5 M was spin-coated on ETL/ITO at 1500 rpm for 30 s, followed by annealing at 70 °C for 60 s. After that, the ammonium salt solution (90.0 mg FAI, 9.0 mg MACl, and 6.4 mg MAI dissolved in 1.0 mL IPA) was then deposited on the PbI_2 films at 2000 rpm for 30 s and subsequently heat-treated at 150 °C for 15 min to gain PVK films. To 1.0 mL of CB, 75.0 mg of spiro-OMeTAD, 28.8 μL of *t*-BP, and 17.5 μL of Li-TFSI solution (520.0 mg of Li-TFSI in 1.0 ml of ACN) were added sequentially and mixed homogeneously to gain the HTL solution. The HTL solution was spin-coated onto the PVK layers at 3500 rpm for 30 s to gain the HTL layers, followed by oxidation at 10% humidity for 12 hours. Finally, a silver electrode with a thickness of 80.0 nm was deposited by the ultra-vacuum thermal evaporation.

4.3 Film characterization

The atomic states and energy level structure changes on the surface of the samples were investigated using the photoelectron spectrometer systems (ESCLAB 250xi, Thermo Scientific) equipped with XPS and UPS. The interactions between substances were also analyzed using nuclear magnetic resonance (AVANCE III 500 MHz, Bruker). The surface properties of the samples were determined by SEM (SU-8000, Hitachi) and AFM (Multimode-8j, Bruker). The crystallinity of the samples was characterized by XRD using Cu Kα radiation (SmartLab, Rigaku). The SSPL intensity was collected using a highly sensitive fluorescence spectrophotometer (LF-1303003, Thermo Scientific). The UV-Vis absorption of the samples was measured with a spectrometer(Lamda 950UV/VIS/NIR, PerkinElmer). The physical parameter E_U can be utilized to quantify the film quality. The correlation between E_U and absorption coefficient (α) can be denoted by the following formula:[38]

$$\alpha = \alpha_0 \exp\frac{Hv}{E_U}$$

where Hv and α_0 correspond to the photon energy and a constant, respectively. A time-dependent single photon counting device (Pico harp 300) was applied to record the TRPL decay on an Omin-k Monochromator/Splitter (Zolix). To analyze the TRPL decay curve, a generally used method is to fit it to a bi-exponential equation, expressed as follows:[24]

$$f(t) = A_1 e^{\frac{-t}{\tau_1}} + A_2 e^{\frac{-t}{\tau_2}} + B$$

where τ_1 corresponds to the fast decay lifetime, τ_2 corresponds to the slow decay lifetime, while A_1 and A_2 are relative amplitudes. The average decay lifetime (τ_{avg}) can be calculated using the following equation:[34]

$$\tau_{avg} = \frac{A_1\tau_1{}^2 + A_2\tau_2{}^2}{A_1\tau_1 + A_2\tau_2}.$$

4.4 Device characterization

For the acquisition of the *J–V* curve of the PSCs, the data were recorded using a Keithley 2420 source meter under AM 1.5G illumination in a solar simulator (Oriel Sol 3A, Newport). The light intensity of simulated sunlight was calibrated using a Si solar cell that is NREL-certified. Meanwhile, the dark *J–V* curves were obtained by measuring the data in a dark environment using the aforementioned method. After obtaining the dark *J–V* curves for electron-only devices, their electron defect density can be analyzed using the SCLC technique. Once the value of V_{TFL} has been determined, the value of N_{trap} can be obtained by employing the following formula:[40]

$$N_{trap} = \frac{2\varepsilon\varepsilon_0 V_{TFL}}{eL^2}$$

where e signifies the electric charge, L signifies the PVK's thickness, ε signifies the PVK's relative permittivity, and ε_0 signifies the vacuum permittivity. Based on the *J–V* curves data recorded under different light intensities (I), the curves of light-intensity-dependent V_{OC} can be plotted. The correlation between I and V_{OC} adheres to the following formula:[40]

$$V_{oc} = \frac{nKT}{e}\ln(I) + \text{constant}$$

where n signifies the ideal coefficient, K signifies the Boltzmann constant, and T signifies the absolute temperature. TPV, *C–V*, *M–S*, and EIS measurements were all performed using an electrochemical workstation (IM6e, Zahner). The built-in electric field can be employed to assess whether charge extraction is difficult or not. The relationship between capacitance (C) and V_{bi} can be expressed by the following equation:[15]

$$\frac{1}{C^2} = \frac{2}{\varepsilon\varepsilon_0 eN_D S^2}(V_{bi} - V)$$

where S and N_D signify the active area and the doping density, respectively. The curves of tDOS can be obtained through angular frequency related capacitance, using the following formula:[42]

$$N_t(E_\omega) = -\frac{\omega}{KT}\frac{V_{bi}}{eW}\frac{dC}{d\omega}$$

where N_t signifies the trap density, E_ω signifies the demarcation energy, ω signifies the angle frequency, and W signifies the depletion width. Based on the applied ω, E_ω can be determined from the following equation:[42]

$$E_\omega = KT\ln\left(\frac{\omega_0}{\omega}\right)$$

where ω_0 signifies the attempt-to-escape frequency.

Data availability

The data that support the findings of this study are available from the corresponding author upon reasonable request.

Conflicts of interest

The authors declare no competing financial interest.

Acknowledgements

This work was financially supported by the project of the National Natural Science Foundation of China (No. 22271106, 51972123, 61804058, U20A20150, and U1705256), Young Elite Scientist Sponsorship Program by Cast of China Association for Science and Technology (YESS20210285), and Guangdong Basic and Applied Basic Research Foundation (2022A1515011613). The authors would like to thank the Instrumental Analysis Center of Huaqiao University for providing SEM, XRD, XPS and UPS characterization.

References

1 F. Fabregat-Santiago, J. Bisquert, L. Cevey, P. Chen, M. Wang, S. M. Zakeeruddin and M. Grätzel, Electron Transport and Recombination in Solid-State Dye Solar Cell with Spiro-OMeTAD as Hole Conductor, *J. Am. Chem. Soc.*, 2009, **131**, 558–562.
2 M. M. Lee, J. Teuscher, T. Miyasaka, T. N. Murakami and H. J. Snaith, Efficient Hybrid Solar Cells Based on Meso-Superstructured Organometal Halide Perovskites, *Science*, 2012, **338**, 643–647.
3 M. Liu, M. B. Johnston and H. J. Snaith, Efficient planar heterojunction perovskite solar cells by vapour deposition, *Nature*, 2013, **501**, 395–398.
4 H. Zhou, Q. Chen, G. Li, S. Luo, T.-B. Song, H.-S. Duan, Z. Hong, J. You, Y. Liu and Y. Yang, Interface engineering of highly efficient perovskite solar cells, *Science*, 2014, **345**, 542–546.
5 W. S. Yang, J. H. Noh, N. J. Jeon, Y. C. Kim, S. Ryu, J. Seo and S. I. Seok, High-performance photovoltaic perovskite layers fabricated through intramolecular exchange, *Science*, 2015, **348**, 1234–1237.
6 M. Abdi-Jalebi, Z. Andaji-Garmaroudi, S. Cacovich, C. Stavrakas, B. Philippe, J. M. Richter, M. Alsari, E. P. Booker, E. M. Hutter, A. J. Pearson, S. Lilliu, T. J. Savenije, H. Rensmo, G. Divitini, C. Ducati, R. H. Friend and S. D. Stranks, Maximizing and stabilizing luminescence from halide perovskites with potassium passivation, *Nature*, 2018, **555**, 497–501.
7 Y. Tu, X. Yang, R. Su, D. Luo, Y. Cao, L. Zhao, T. Liu, W. Yang, Y. Zhang, Z. Xu, Q. Liu, J. Wu, Q. Gong, F. Mo and R. Zhu, Diboron-Assisted Interfacial Defect Control Strategy

for Highly Efficient Planar Perovskite Solar Cells, *Adv. Mater.*, 2018, **30**, 1805085.

8 Y. Yang, J. Wu, X. Wang, Q. Guo, X. Liu, W. Sun, Y. Wei, Y. Huang, Z. Lan, M. Huang, J. Lin, H. Chen and Z. Wei, Suppressing Vacancy Defects and Grain Boundaries via Ostwald Ripening for High-Performance and Stable Perovskite Solar Cells, *Adv. Mater.*, 2020, **32**, 1904347.

9 Q. Xiong, C. Wang, Q. Zhou, L. Wang, X. Wang, L. Yang, J. Ding, C.-C. Chen, J. Wu, X. Li and P. Gao, Rear Interface Engineering to Suppress Migration of Iodide Ions for Efficient Perovskite Solar Cells with Minimized Hysteresis, *Adv. Funct. Mater.*, 2022, **32**, 2107823.

10 Q. Guo, J. Duan, J. Zhang, Q. Zhang, Y. Duan, X. Yang, B. He, Y. Zhao and Q. Tang, Universal Dynamic Liquid Interface for Healing Perovskite Solar Cells, *Adv. Mater.*, 2022, **34**, 2202301.

11 X. Zhang, X. Li, L. Tao, Z. Zhang, H. Ling, X. Fu, S. Wang, M. J. Ko, J. Luo, J. Chen and Y. Li, Precise Control of Crystallization and Phase-Transition with Green Anti-Solvent in Wide-Bandgap Perovskite Solar Cells with Open-Circuit Voltage Exceeding 1.25 V, *Small*, 2023, **19**, 2208289.

12 J. Park, J. Kim, H.-S. Yun, M. J. Paik, E. Noh, H. J. Mun, M. G. Kim, T. J. Shin and S. I. Seok, Controlled growth of perovskite layers with volatile alkylammonium chlorides, *Nature*, 2023, **616**, 724–730.

13 S. Y. Park and K. Zhu, Advances in SnO_2 for Efficient and Stable n-i-p Perovskite Solar Cells, *Adv. Mater.*, 2022, **34**, 2110438.

14 T. Zhang, Q. He, J. Yu, A. Chen, Z. Zhang and J. Pan, Recent progress in improving strategies of inorganic electron transport layers for perovskite solar cells, *Nano Energy*, 2022, **104**, 107918.

15 T. Yang, L. Gao, J. Lu, C. Ma, Y. Du, P. Wang, Z. Ding, S. Wang, P. Xu, D. Liu, H. Li, X. Chang, J. Fang, W. Tian, Y. Yang, S. Liu and K. Zhao, One-stone-for-two-birds strategy to attain beyond 25% perovskite solar cells, *Nat. Commun.*, 2023, **14**, 839.

16 Y. Chen, Q. Wang, W. Tang, W. Qiu, Y. Wu and Q. Peng, Heterocyclic amino acid molecule as a multifunctional interfacial bridge for improving the efficiency and stability of quadruple cation perovskite solar cells, *Nano Energy*, 2023, **107**, 108154.

17 L. Yang, H. Zhou, Y. Duan, M. Wu, K. He, Y. Li, D. Xu, H. Zou, S. Yang, Z. Fang, S. Liu and Z. Liu, 25.24%-Efficiency $FACsPbI_3$ Perovskite Solar Cells Enabled by Intermolecular Esterification Reaction of DL-Carnitine Hydrochloride, *Adv. Mater.*, 2023, **35**, 2211545.

18 Y. Dong, W. Shen, W. Dong, C. Bai, J. Zhao, Y. Zhou, F. Huang, Y.-B. Cheng and J. Zhong, Chlorobenzenesulfonic Potassium Salts as the Efficient Multifunctional Passivator for the Buried Interface in Regular Perovskite Solar Cells, *Adv. Energy Mater.*, 2022, **12**, 2200417.

19 L. Fu, H. Li, L. Wang, R. Yin, B. Li and L. Yin, Defect passivation strategies in perovskites for an enhanced photovoltaic performance, *Energy Environ. Sci.*, 2020, **13**, 4017–4056.

20 C. Deng, J. Wu, Y. Yang, Y. Du, R. Li, Q. Chen, Y. Xu, W. Sun, Z. Lan and P. Gao, Modulating Residual Lead Iodide via Functionalized Buried Interface for Efficient and Stable Perovskite Solar Cells, *ACS Energy Lett.*, 2023, **8**, 666–676.

21 F. Gao, C. Luo, X. Wang, C. Zhan, Y. Li, Y. Li, Q. Meng, M. Yang, K. Su, D. Yuan, R. Zhu and Q. Zhao, Porous Organic Cage Induced Spontaneous Restructuring of Buried Interface Toward High-Performance Perovskite Photovoltaic, *Adv. Funct. Mater.*, 2023, **33**, 2211900.

22 Z. Ni, C. Bao, Y. Liu, Q. Jiang, W.-Q. Wu, S. Chen, X. Dai, B. Chen, B. Hartweg, Z. Yu, Z. Holman and J. Huang, Resolving spatial and energetic distributions of trap states in metal halide perovskite solar cells, *Science*, 2020, **367**, 1352–1358.

23 M. Stolterfoht, C. M. Wolff, J. A. Márquez, S. Zhang, C. J. Hages, D. Rothhardt, S. Albrecht, P. L. Burn, P. Meredith, T. Unold and D. Neher, Visualization and suppression of interfacial recombination for high-efficiency large-area pin perovskite solar cells, *Nat. Energy*, 2018, **3**, 847–854.

24 J. Chen, X. Zhao, S.-G. Kim and N.-G. Park, Multifunctional Chemical Linker Imidazoleacetic Acid Hydrochloride for 21% Efficient and Stable Planar Perovskite Solar Cells, *Adv. Mater.*, 2019, **31**, 1902902.

25 S. You, H. Zeng, Z. Ku, X. Wang, Z. Wang, Y. Rong, Y. Zhao, X. Zheng, L. Luo, L. Li, S. Zhang, M. Li, X. Gao and X. Li, Multifunctional Polymer-Regulated SnO_2 Nanocrystals Enhance Interface Contact for Efficient and Stable Planar Perovskite Solar Cells, *Adv. Mater.*, 2020, **32**, 2003990.

26 Q. Zhou, D. He, Q. Zhuang, B. Liu, R. Li, H. Li, Z. Zhang, H. Yang, P. Zhao, Y. He, Z. Zang and J. Chen, Revealing Steric-Hindrance-Dependent Buried Interface Defect Passivation Mechanism in Efficient and Stable Perovskite Solar Cells with Mitigated Tensile Stress, *Adv. Funct. Mater.*, 2022, **32**, 2205507.

27 J. Deng, H. Zhang, K. Wei, Y. Xiao, C. Zhang, L. Yang, X. Zhang, D. Wu, Y. Yang and J. Zhang, Molecular Bridge Assisted Bifacial Defect Healing Enables Low Energy Loss for Efficient and Stable Perovskite Solar Cells, *Adv. Funct. Mater.*, 2022, **32**, 2209516.

28 C. Kan, Z. Tang, Y. Yao, P. Hang, B. Li, Y. Wang, X. Sun, M. Lei, D. Yang and X. Yu, Mitigating Ion Migration by Polyethylene Glycol-Modified Fullerene for Perovskite Solar Cells with Enhanced Stability, *ACS Energy Lett.*, 2021, **6**, 3864–3872.

29 Z. Wang, Q. Tian, H. Zhang, H. Xie, Y. Du, L. Liu, X. Feng, A. Najar, X. Ren and S. Liu, Managing Multiple Halide-Related Defects for Efficient and Stable Inorganic Perovskite Solar Cells, *Angew. Chem., Int. Ed.*, 2023, **62**, e202305815.

30 Y. Che, Z. Liu, Y. Duan, J. Wang, S. Yang, D. Xu, W. Xiang, T. Wang, N. Yuan, J. Ding and S. Liu, Hydrazide Derivatives for Defect Passivation in Pure $CsPbI_3$ Perovskite Solar Cells, *Angew. Chem., Int. Ed.*, 2022, **61**, e202205012.

31 X. Wang, D. Liu, R. Liu, X. Du, B. Zhang, X. Sun, C. Chen, Z. Li, Q. Zhao, Z. Shao, X. Wang, G. Cui and S. Pang, PbI_6 Octahedra Stabilization Strategy Based on π-π Stacking Small Molecule Toward Highly Efficient and Stable Perovskite Solar Cells, *Adv. Energy Mater.*, 2023, **13**, 2203635.

32 Z. Xu, N. Liu, X. Liu, W. Han, W. Xu, J. Zhang, L. Huang, Z. Hu and Y. Zhu, Multifunctional alkylamines enable defect passivation and energy level alignment for efficient and stable inverted $CsPbI_3$ perovskite solar cells, *Chem. Eng. J.*, 2023, **451**, 139047.

33 L. Zhang, K. Cao, J. Qian, Y. Huang, X. Wang, M. Ge, W. Shen, F. Huang, M. Wang, W. Zhang, S. Chen and T. Qin, Crystallization control and multisite passivation of perovskites with amino acid to boost the efficiency and stability of perovskite solar cells, *J. Mater. Chem. C*, 2020, **8**, 17482–17490.

34 Z. Xiong, X. Chen, B. Zhang, G. O. Odunmbaku, Z. Ou, B. Guo, K. Yang, Z. Kan, S. Lu, S. Chen, N. A. N. Ouedraogo, Y. Cho, C. Yang, J. Chen and K. Sun, Simultaneous Interfacial Modification and Crystallization Control by Biguanide Hydrochloride for Stable Perovskite Solar Cells with PCE of 24.4%, *Adv. Mater.*, 2022, **34**, 2106118.

35 Y. Zhou, Z. Wang, J. Jin, X. Zhang, J. Zou, F. Yao, Z. Zhu, X. Cui, D. Zhang, Y. Yu, C. Chen, D. Zhao, Q. Cao, Q. Lin and Q. Tai, Manipulation of the Buried Interface for Robust Formamidinium-based Sn-Pb Perovskite Solar Cells with NiOx Hole-Transport Layers, *Angew. Chem., Int. Ed.*, 2023, **62**, e202300759.

36 G. Li, J. Song, J. Wu, Z. Song, X. Wang, W. Sun, L. Fan, J. Lin, M. Huang, Z. Lan and P. Gao, Efficient and Stable 2D@3D/2D Perovskite Solar Cells Based on Dual Optimization of Grain Boundary and Interface, *ACS Energy Lett.*, 2021, **6**, 3614–3623.

37 D. Yang, R. Yang, K. Wang, C. Wu, X. Zhu, J. Feng, X. Ren, G. Fang, S. Priya and S. Liu, High efficiency planar-type perovskite solar cells with negligible hysteresis using EDTA-complexed SnO_2, *Nat. Commun.*, 2018, **9**, 3239.

38 C.-H. Chen, F. Hu, Z.-H. Su, Y.-J. Yu, K.-L. Wang, Y.-R. Shi, J. Chen, Y. Xia, X.-Y. Gao, Z.-K. Wang and L.-S. Liao, Spring-Like Ammonium Salt Assisting Stress Release for Low-Temperature Deposited $FAPbI_3$ Films Toward Flexible Photovoltaic Application, *Adv. Funct. Mater.*, 2023, **33**, 2213661.

39 P. Chen, W. Pan, S. Zhu, F. Cao, A. Tong, R. He, Z. Lan, W. Sun and J. Wu, Buried modification with tetramethylammonium chloride to enhance the performance of perovskite solar cells with n-i-p structure, *Chem. Eng. J.*, 2023, **468**, 143652.

40 W. Pan, J. Lin, J. Wu, X. Wang, G. Li, Y. Du, W. Li, W. Sun and Z. Lan, Efficient surface treatment based on an ionic imidazolium hexafluorophosphate for improving the efficiency and stability of perovskite solar cells, *Appl. Surf. Sci.*, 2022, **604**, 154486.

41 X. Zheng, B. Chen, J. Dai, Y. Fang, Y. Bai, Y. Lin, H. Wei, X. C. Zeng and J. Huang, Defect passivation in hybrid perovskite solar cells using quaternary ammonium halide anions and cations, *Nat. Energy*, 2017, **2**, 17102.

42 J. Zhang, S. Wu, T. Liu, Z. Zhu and A. K.-Y. Jen, Boosting Photovoltaic Performance for Lead Halide Perovskites Solar Cells with BF_4^- Anion Substitutions, *Adv. Funct. Mater.*, 2019, **29**, 1808833.

